applied sciences

MDPI

Article

Numerical Simulation of Flow Field of Submerged Angular Cavitation Nozzle

Wenqiang Dong, Ligang Yao * and Weilin Luo

College of Mechanical Engineering and Automation, Fuzhou University, Fuzhou 350108, China
* Correspondence: ylgyao@fzu.edu.cn

Abstract: A model of a submerged angular cavitation nozzle is established, which consists of a contraction part, parallel middle part, and expansion part. Based on the CFD technique, a numerical simulation of the flow field of the submerged cavitation nozzle is carried out, in which a multiphase mixture model, cavitation model, and renormalization group (RNG) k-ε turbulence model are applied. Considering the influence of mixture density on cavitation, the effects of the inlet contraction part, parallel middle part, and outlet expansion part on the velocity and vapor volume fraction are studied. The numerical simulation results show that the mixture density is essential in the cavitation jet. When the nozzle diameter d is fixed, the designed angular cavitation nozzle with contraction angle $\alpha = 13.5°$, parallel middle part length $Ld = 3d$, expansion part length $Le = 4d$, and expansion angle $\beta = 60°$ can effectively bring out cavitation. A cavitation cloud is produced near the rigid wall of the outlet expansion section and diffuses in a vortex ring shape. Optimizing the nozzle structure can improve the cavitation effect of the nozzle. The feasibility of this model is verified by relevant experimental data.

Keywords: cavitation jet; angular cavitation nozzle; submerged environment; numerical simulation

check for updates

Citation: Dong, W.; Yao, L.; Luo, W. Numerical Simulation of Flow Field of Submerged Angular Cavitation Nozzle. *Appl. Sci.* **2023**, *13*, 613. https://doi.org/10.3390/app13010613

Academic Editor: Luís L. Ferrás

Received: 5 December 2022
Revised: 23 December 2022
Accepted: 27 December 2022
Published: 2 January 2023

Copyright: © 2023 by the authors. Licensee MDPI, Basel, Switzerland. This article is an open access article distributed under the terms and conditions of the Creative Commons Attribution (CC BY) license (https://creativecommons.org/licenses/by/4.0/).

1. Introduction

Cavitation water jet technology is one of the effective fouling prevention methods that has received widespread attention in recent years [1–3]. It has the advantages of energy saving and environmental protection, high cleaning efficiency, no damage to equipment surfaces, and easy mechanization and automation. A representative application example of the cavitation water jet is underwater organism removal [4,5].

Issues on cavitation water jets mainly concern water jet flow characteristics, cavitation nozzle optimization, and erosion performance enhancement. In general, the analysis of cavitation water jets is carried out by experiments and numerical simulation. Through experiments, the performance of cavitation nozzles can be enhanced not only by observing the erosion effect [6,7] but also by visualization through high-speed photography and acoustic emission [8]. Hutli et al. [9] established cavitation efficiency expressions, and the experimental analysis showed that the nozzle diameter and injection distance have a large effect on the kinetic energy and specific energy consumption. Li et al. [10] used the frame-difference method to analyze the dynamic evolution of the cavitation cloud and obtain the range of concentrated cavitation collapse. The best target distance range was determined by the verification test of cavitation water blasting of 2A12 aluminum alloy. Wang et al. [11] established a high-pressure cavitation jet experimental system and conducted high-speed photographic experiments. It was found that the periodic time–frequency of cavitation development could be better reflected by the proper orthogonal decomposition (POD) method. Jablonská et al. [12] concluded that the mixture composition of the flowing medium (liquid, steam, and air) has a particular influence on the size and pulsation frequency of the cavitation cloud by observing the dynamic behavior of the cavitation cloud in the flow of a converging–diffusing nozzle with a rectangular cross-section. Mitroglou et al. [13] used high-speed imaging to characterize the development and

collapse of the cavitation cloud inside the nozzle and its connection with surface erosion, showing that cavitation vortex shedding occurs in a periodic manner. Ibanez et al. [14] evaluated the cavitation effect by measuring the specimen weight change, showing that acoustic emission monitoring is a promising tool.

As an effective supplement to research tools, numerical simulation by means of computers can reproduce experimental scenarios without laboriously setting up the experimental platform. Numerical simulation can also yield accurate results and, therefore, is favored by researchers. In the research on cavitation water jet based on numerical simulation, Yang et al. [15] conducted a numerical study of the underwater high-pressure cavitation water jet with Reynolds-averaged Navier–Stokes (RANS)–large eddy simulation (LES) hybrid model to reveal the relationship between the shear cavitation formation mechanism and the turbulence structure and velocity distribution characteristics in the jet. Ran et al. [16] used a mass transfer cavitation model and a modified RANS k-ω model to study the structure of cavitation nozzles under various operating conditions, revealing that the re-entrant jet is the main cause of shedding cavitation and destruction of O-type cavitation. Kumar et al. [17] predicted the jet flow by the Zwart–Gerber–Belamri (ZGB) model and found that simulation results using compressible assumptions are in better quantitative and qualitative agreement with experimental data. Chen et al. [18] developed a hybrid optimization algorithm combined with CFD techniques to improve the cavitation effect of nozzles in deep water. Wu et al. [19] studied the effect of differently shaped nozzles on cavitation performance, and the numerical simulation results showed that the hydraulic diameter at the nozzle outlet has a high correlation with the gas phase distribution after cavitation. Wang et al. [20] used a two-equation curve to determine the outdoor profile of the nozzle cavity based on the Helmholtz nozzle, and the experimental analysis results showed that the designed nozzle had good flushing efficiency. Zhang et al. [21] developed a nozzle of swirling cavitating jet for natural gas hydrate, and the experimental results confirmed the flow field characteristics and erosion performance of the nozzle. Omelyanyuk et al. [22] compared the CFD calculation results using the RANS SST k-ω turbulence model with the experimental results and found that the cavitation onset was sensitive to the nozzle geometry. The cavitation onset may be different for the same cavitation number.

However, the above literature focuses on improving the accuracy of numerical models to observe the subtle flow of water jets, which not only improves the accuracy of results but also increases the difficulty of calculation. This is helpful to the theoretical development of fluid mechanics but neglects the optimization of the nozzle structure in engineering applications. In practical applications, the nozzle needs to be optimized in advance by numerical simulation and then installed by a target distance experiment. Therefore, the numerical simulation should have a certain precision but not time-consuming calculation.

If the physical properties of the jet are the same as those of the surrounding medium, it is a submerged jet; if not, it is a nonsubmerged jet [23]. In general, the submerged jet with water as the fluid medium refers to the underwater jet. The cavitation nozzle, as a cavitation-generating element, directly affects the cavitation effect of the jet [24]; thus, it is significant to carry out research on it. Although the existing literature has discussed the jet and cavitation characteristics of the cavitation nozzle under submerged and nonsubmerged conditions, the focus is mostly on the accuracy of the model, and the optimization of the nozzle structure has no practical application. In this paper, we have designed and optimized a cavitation nozzle for underwater creature removal and established the three-dimensional (3D) physical model of the angular cavitation nozzle in the submerged state by using CFX fluid simulation software. The main purpose of the study is to optimize the structure of the cavitation nozzle by using the CFD technique. The effect of mixture density on cavitation is orderly discussed under the multiphase mixture model. The feasibility of this model is verified by relevant experimental data. Then, the velocity distribution, pressure distribution, and vapor volume fraction distribution of the flow field inside and outside the nozzle in the computational domain could be derived by solving the RNG *k*-ε model and homogeneous cavitation model. We aimed to investigate in depth the effect of

the nozzle inlet contraction section, cylindrical section, and outlet expansion section on the cavitation effect of the jet in the submerged state, to improve the degree of cavitation of the angular cavitation nozzle, and to provide a basis for the study of water jet cavitation.

2. Numerical Calculation Method

2.1. Physical Model of Angular Cavitation Nozzle

The physical model of the angular cavitation nozzle is composed of four parts: the inlet contraction section, the cylinder section, the outlet expansion section, and the external flow field cylinder, as shown in Figure 1. The length *a* of the external flow field cylinder is 20 mm, and the diameter *b* is 40 mm. The structure of the angular cavitation nozzle is used for the classical "leach & walker" model [14]. On this basis, the length *Lc* of the nozzle contraction section is uniformly set to 26 mm, and then the diameter *d* of the cylinder section is set to 2.5 mm according to the rated pressure of 20 MPa and the rated flow of 43 L/min of the high-pressure piston pump, and the other nozzle structural parameters are designed to analyze the nozzle contraction angle α, length *Ld* of the cylindrical section, length *Le* of the expansion section, and expansion angle β on the effect of jet cavitation. For the authenticity of the simulation, a 3D model is used.

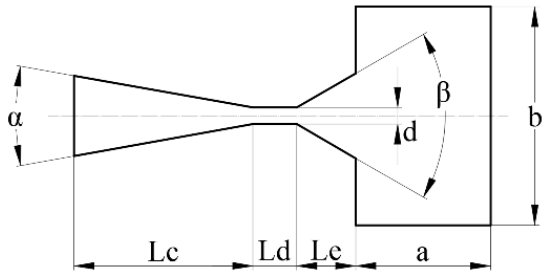


Figure 1. Schematic diagram of physical model.

2.2. Mathematical Model of Angular Cavitation Nozzle

The mathematical models of the angular cavitation nozzle include the multiphase flow mixture model, cavitation model, and RNG *k*-ε turbulence model [25], which must satisfy the momentum conservation equation, continuity equation, and relevant model equations.

2.2.1. Multiphase Flow Mixture Model

The cavitation jet belongs to a gas–liquid two-phase flow, and a reference analysis [26] shows that for the current nozzle flow, the relative motion of the two phases can be ignored, so we consider the vapor–liquid flow to be a uniform bubble–liquid mixture. The nozzle flow simulations can be performed using the homogeneous equilibrium model. For the mixture model, the basic equations of continuity and momentum are the same as those in single-phase flow except that the density and dynamic viscosity in the cavitating flow of nozzles use the mixture density ρ and the mixture dynamic viscosity μ:

$$\rho = r_l\rho_l + r_v\rho_v \tag{1}$$

$$\mu = r_l\mu_l + r_v\mu_v \tag{2}$$

where r_l is the volume fraction of the liquid, r_v is the volume fraction of the vapor, $r_l + r_v = 1$, ρ_l is the density of the liquid, ρ_v is the density of the vapor, μ_l is the dynamic viscosity of the liquid, and μ_v is the dynamic viscosity of the vapor. The mixture velocity vector $\boldsymbol{U}$ is as follows:

$$\boldsymbol{U} = \frac{1}{\rho}(r_l\rho_l\boldsymbol{U}_l + r_v\rho_v\boldsymbol{U}_v) \tag{3}$$

where $\boldsymbol{U}_l$ is the velocity vector of the liquid and $\boldsymbol{U}_v$ is the velocity vector of the vapor. Thus, assuming an incompressible liquid, the momentum conservation equation and continuity equation of cavitation flow are as follows:

$$\rho\frac{\partial \boldsymbol{U}}{\partial t} + \rho\boldsymbol{U}\cdot\nabla\boldsymbol{U} = -\nabla p + \mu\nabla^2\boldsymbol{U} \tag{4}$$

$$\frac{\partial \rho}{\partial t} + \nabla\cdot(\rho\boldsymbol{U}) = 0 \tag{5}$$

where p is the peripheral pressure.

Experimental observations show that cavitation caused in the high-speed submerged water jet appears in the form of a bubble cloud [27]. Corresponding to the variation of surrounding liquid pressure, bubble clouds expand and break up unsteadily. Thus, the density of the two-phase mixture varies sharply with bubble oscillation, and it becomes essential to consider the effect of fluid compressibility in the numerical simulation of intensive cavitating flows.

When considering the compressibility of the mixture, from the conservation of mass, Equation (1) can be derived as:

$$\rho \mathrm{d}V = r_l\rho_l \mathrm{d}V_l + r_v\rho_v \mathrm{d}V_v \tag{6}$$

where $\mathrm{d}V$ is assumed as the change in total volume and $\mathrm{d}V_l$ and $\mathrm{d}V_v$ are the volume changes of fluid and gas, respectively. Further, the result can be written as:

$$\frac{1}{\rho}\mathrm{d}\rho = \frac{r_l}{\rho_l}\mathrm{d}\rho_l + \frac{r_v}{\rho_v}\mathrm{d}\rho_v \tag{7}$$

In accordance with the definition of sonic velocity, Equation (7) is expressed as follows:

$$\frac{1}{\rho c^2}\mathrm{d}p = \frac{r_l}{\rho_l c_l^2}\mathrm{d}p_l + \frac{r_v}{\rho_v c_v^2}\mathrm{d}p_v \tag{8}$$

where c is the sonic velocity of a mixture, c_l is the sonic velocity of the fluid, and c_v is the sonic velocity of the vapor. In the absence of surface tension, according to a local equilibrium state, one obtains that $p = p_l = p_v$. Hence, the sonic velocity of the mixture is given by:

$$\frac{1}{\rho c^2} = \frac{r_l}{\rho_l c_l^2} + \frac{r_v}{\rho_v c_v^2} \tag{9}$$

In other words, the acoustic impedance $1/\rho c^2$ for the mixture is simply given by the average of the acoustic impedance of the components weighted according to their volume fractions. Supposing the gas is perfect and the process is isentropic,

$$\rho_v c_v^2 = k p_v \tag{10}$$

where k is the adiabatic index and p_v is the gas pressure. Therefore, Equation (9) may be written as:

$$\frac{1}{\rho c^2} = \frac{r_l}{\rho_l c_l^2} + \frac{r_v}{k p_v} \tag{11}$$

Note that, in most applications, dramatic effects occur when one of the components is a vapor, which is much more compressible than the other component such as liquid. Hence, the above expression may be further simplified to:

$$\frac{1}{\rho c^2} = \frac{r_v}{k p_v} \tag{12}$$

It can also be expressed as:

$$\frac{1}{c^2} = \frac{r_v}{kp_v}((1 - r_v)\rho_l + r_v\rho_v) \tag{13}$$

This is the case of a homogeneous two-phase mixture, and it may be similar to the one given by Brenenn [26]. It obviously follows that the sonic velocity of a mixture can be much smaller than that of either of its constituents.

Figure 2 shows the sonic speed in a bubbly mixture evaluated by Equation (13) against different gas volume fractions. The circles demonstrate the instance of bubble cavitation under atmospheric pressure when T = 293.15 K, which is the experimental data of Karplus [27]. The velocity of sound in a homogeneous mixture is denoted by various curves, which correspond to different pressures. One at p = 0.1 MPa agrees with the experimental data. The figure demonstrates that the sound velocity in the cavitation bubble–liquid mixture attenuation is very obvious. Hence, it should be essential to estimate the mixture compressibility by considering the effect of bubble dynamics in the numerical simulation of intensive cavitating flow with the mixture flow method.

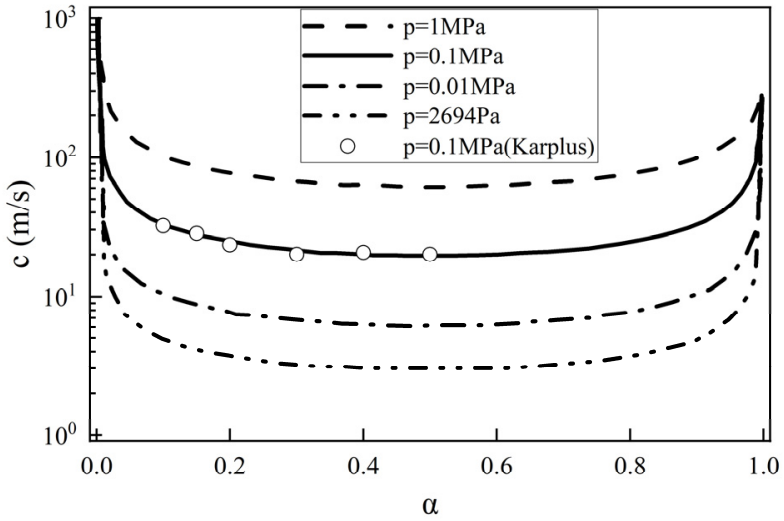


Figure 2. The sonic velocity of mixture under vapor volume fraction.

2.2.2. Cavitation Model

The cavitation model is used to describe the mass transfer mechanism between the two vapor–liquid phases. It treats the bubbly flow as a homogeneous vapor–liquid mixture and assumes that the vapor phase consists of numerous tiny spherical bubbles. The model uses the Rayleigh–Plesset equation for the description of bubble growth and collapse [26]:

$$R\frac{\mathrm{d}^2R}{\mathrm{d}t^2} + \frac{3}{2}\left(\frac{\mathrm{d}R}{\mathrm{d}t}\right)^2 = \frac{1}{\rho_f}\left(p_g - p_\infty + \frac{2\sigma}{R}\right) \tag{14}$$

where R is the bubble radius, p_g is the pressure in the bubble (assumed to be the saturated vapor pressure at the temperature of the liquid), p_∞ is the pressure in the liquid surrounding the bubble, ρ_f is the density of the liquid, and σ is the surface tension coefficient between the liquid and the gas. Neglecting second-order terms (which is suitable for low vibration frequencies) and surface tension, this equation can be reduced to:

$$\frac{\mathrm{d}R}{\mathrm{d}t} = \sqrt{\frac{2}{3}\frac{|p_g - p_\infty|}{\rho_f}} \tag{15}$$

The rate of change in the mass of the bubble is:

$$\frac{\mathrm{d}m}{\mathrm{d}t} = \rho_g \frac{\mathrm{d}V}{\mathrm{d}t} = \rho_g \frac{\mathrm{d}}{\mathrm{d}t}\left(\frac{4}{3}\pi R^3\right) = \rho_g \pi R^2 \sqrt{\frac{2}{3}\frac{|p_g - p_\infty|}{\rho_f}} \tag{16}$$

where ρ_g is the density of the vapor and V is the volume of the bubble. If N_B is the number of bubbles per unit volume, the volume fraction r_g can be expressed as:

$$r_g = VN_B = \frac{4}{3}\pi R^3 N_B \tag{17}$$

The total rate of interphase to phase mass transfer per unit volume is:

$$M = N_B \frac{\mathrm{d}m}{\mathrm{d}t} = \frac{3r_g\rho_g}{\mathrm{R}} \sqrt{\frac{2}{3}\frac{|p_g - p_\infty|}{\rho_f}}\, \mathrm{sgn}(p_v - p_\infty) \tag{18}$$

The cavitation mass transfer process usually includes condensation and evaporation, and their transfer rates are different; thus, Equation (18) could be further optimized as follows:

$$M_{fg} = F_{vap}\frac{3r_{nuc}(1 - r_g)\rho_g}{R_B} \sqrt{\frac{2}{3}\frac{p_v - p_\infty}{\rho_f}} \tag{19}$$

$$M_{gf} = F_{cond}\frac{3r_g\rho_g}{R_B} \sqrt{\frac{2}{3}\frac{p_\infty - p_v}{\rho_f}} \tag{20}$$

where R_B is the radius of the cavitation nucleus, r_{nuc} is the empirical constant, F_{vap} is the evaporation coefficient, and F_{cond} is the condensation coefficient. The default parameters of CFX are set as $R_B = 1$ μm, $r_{nuc} = 5 \times 10^{-4}$, $F_{vap} = 50$, and $F_{cond} = 0.01$. Hence, the cavitation mass transfer rate between the vapor and fluid is governed by the transport equation:

$$\frac{\partial}{\partial t}(r_\theta \rho_\theta) + \nabla \cdot (r_\theta \rho_\theta \boldsymbol{U}_\theta) = \left|M_{fg} - M_{gf}\right| \tag{21}$$

where r_θ is the single-phase volume fraction, ρ_θ is the single-phase density, and $\boldsymbol{U}_\theta$ is the single-phase velocity vector.

2.2.3. Turbulence Model

At present, the Reynolds-averaged Navier–Stokes equations (RANS) method, large eddy simulation (LES) method, and direct numerical simulation (DNS) method are usually used to deal with turbulence problems. The RANS method is the most widely used turbulence numerical simulation method for fluid simulation because of its high computational efficiency and solution accuracy [28]. The *k*-ε model is often used in the simulation of cavitation jets [29]. Three *k*-ε models are provided in CFX software: the standard *k*-ε model and the RNG *k*-ε model.

The standard *k*-ε model has the advantages of wide application scope, economy, and better accuracy. The model assumes that the flow is completely turbulent, and the influence of molecular viscosity can be ignored, so the standard *k*-ε model is only suitable for the simulation of a completely turbulent flow process [29]. The RNG *k*-ε model is added to a condition in ε, taking into account the rotation and flow conditions in the flow, which can better deal with flow with a high strain rate and greater streamline curvature.

Combined with the same model and numerical simulation scheme, two turbulence models are used to characterize the cavitation jet flow field, and the results are shown in Figure 3. From the analysis of the boundary layer, the RNG *k*-ε model has a good analysis of the expansion part.

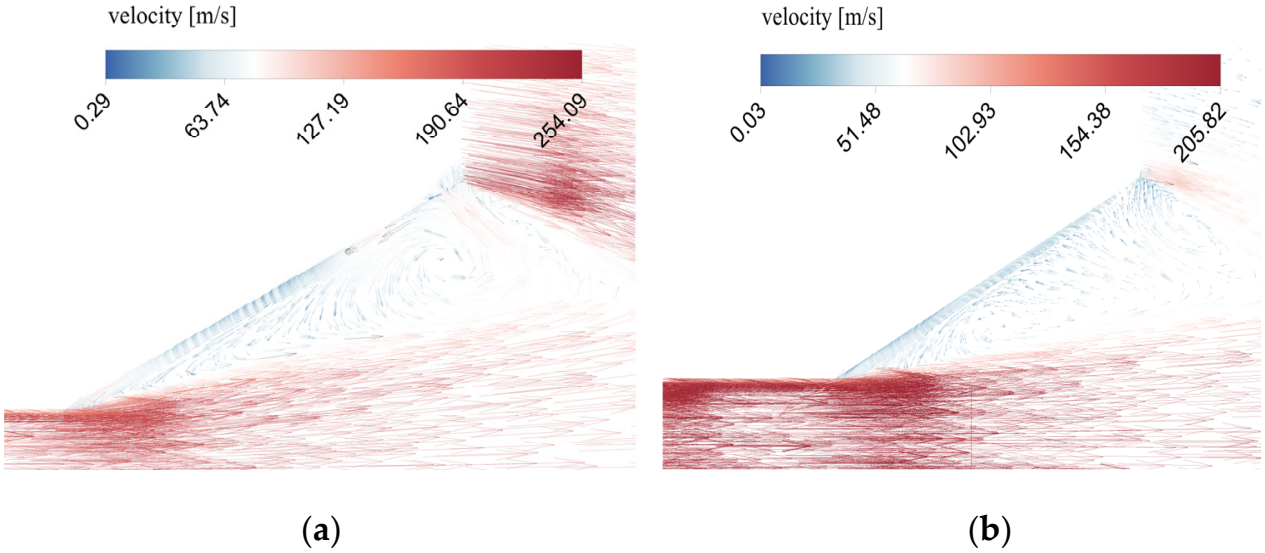


Figure 3. Velocity vector contour on expansion part. (**a**) The standard model; (**b**) the RNG model.

The water jet velocity of the nozzle can be simply calculated by the following Equation [30]:

$$v_t = 44.77\sqrt{p_1} \tag{22}$$

where v_t is the jet velocity and p_1 is the jet incidence pressure. The axial velocity of the RNG model is closer to the theoretical calculation value of 200 m/s (Figure 3). Hence, the RNG k-ε model is a relatively suitable model with high accuracy and fast convergence rate.

The used RNG k-ε model is a RANS-based turbulence model which is in the light of Navier–Stokes equations. For the standard k-ε model cannot accurately predict the impact of transient flow and bending streamline, the RNG k-ε model can reduce the calculation error to a certain extent and expand its field of application by modifying the turbulent dynamic viscosity coefficient [24].

In homogeneous multiphase flow, bulk turbulence equations are solved, which are the same as the single-phase equations except that the mixture density and the mixture viscosity are used. In addition to the dynamic viscosity μ_0 of the fluid itself, turbulence flow usually has a turbulent viscosity μ_t due to its own flow properties:

$$\mu_t = C_\mu \rho_k \frac{k^2}{\varepsilon} \tag{23}$$

where ρ_k is the fluid density, k is the turbulent kinetic energy (the variance of velocity fluctuations), ε is the turbulent vortex dissipation rate (the rate of dissipation of velocity fluctuations), and C_μ is the correction factor. Then, the turbulent effective viscosity μ_{eff} can be obtained by:

$$\mu_{\text{eff}} = \mu_0 + \mu_t \tag{24}$$

Denoting the shear production of turbulence by P_k for convenience:

$$P_k = \mu_t \left(\frac{\partial u_i}{\partial x_j} + \frac{\partial u_j}{\partial x_i} \right) \frac{\partial u_j}{\partial x_i} \tag{25}$$

Hence, the governing equation of the turbulence model is shown in the following equations:

$$\frac{\partial(\rho_k k)}{\partial t} + \frac{\partial(\rho_k k u_i)}{\partial x_i} = \frac{\partial}{\partial x_i} \left(\alpha_k \mu_{\text{eff}} \frac{\partial k}{\partial x_i} \right) + P_k - \rho_k \varepsilon (i, j = 1, 2) \tag{26}$$

$$\frac{\partial(\rho_k \varepsilon)}{\partial t} + \frac{\partial(\rho_k \varepsilon u_i)}{\partial x_i} = \frac{\partial}{\partial x_i}\left(\alpha_e \mu_{\text{eff}} \frac{\partial \varepsilon}{\partial x_i}\right) + \frac{\varepsilon}{k}(C_{\varepsilon 1} P_k - C_{\varepsilon 2} \rho_k \varepsilon) \tag{27}$$

where u_i is the pulsating velocity component in turbulent flow and α_k, α_e, $C_{\varepsilon 1}$, $C_{\varepsilon 2}$ are the model coefficients.

2.3. Meshing

The grid partition of the 3D nozzle model was achieved in the special preprocessor software Mesh. The 3D physical model of the nozzle is globally divided into unstructured mesh, and it adopts the Inflation expansion operation near its solid wall surface. In order to ensure the calculation effect and reduce the amount of calculation, the mesh is encrypted for the focused research areas of the nozzle and water jet flow field such as the nozzle inlet, cylindrical section, and outlet expansion section. The grid division model is shown in Figure 4.

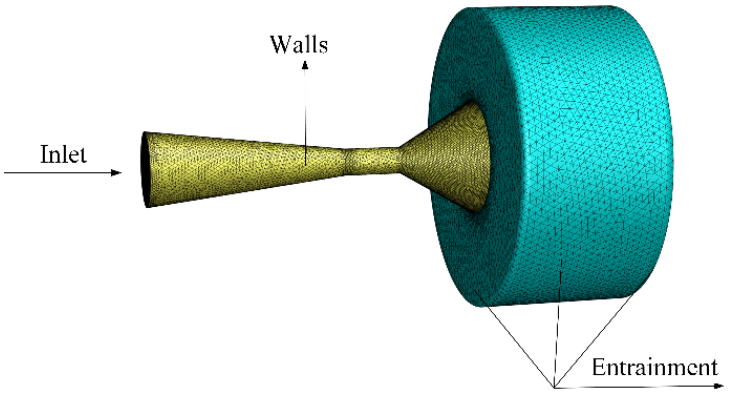


Figure 4. Mesh of calculation domain.

When using Inflation for wall boundary layer grid generation, it is necessary to give priority to the thickness of the first layer of the grid. It is considered that the cavitation jet is a high-Reynolds-number flow, so the high-Reynolds-number scheme is adopted to calculate the boundary layer by using the wall function. According to the selected RNG k-ε turbulence model, the scalable wall function is provided in CFX. In this case, the grid nodes of the first layer are required to be in the region of turbulence, that is, the value of y^+ is between 30 and 300. Assuming that y^+ is 30, the height of the grid in the first layer can be obtained according to the formula [30]:

$$y^+ = \frac{\rho_w u_\tau \Delta y}{\mu_w} \tag{28}$$

where Δy is the distance of the first grid point off the wall and ρ_w, u_τ, and μ_w are the density, friction velocity, and molecular viscosity at the wall, respectively. Hence, the first grid length normal to the wall is 0.01 mm. The CFD postprocessing diagram after convergence is shown in Figure 5. The value of y^+ is within a reasonable range, so the height of the grid in the first layer can be considered justified.

For the abovementioned grid division strategy, grids with different refinements were used to verify the grid independence. The highest vapor fraction and the highest jet velocity in the nozzle are shown in Figure 6 for different mesh numbers. It can be seen that the vapor fraction and jet velocity tend to a stable value when the mesh number exceeds 600,000. Considering the computational and calculation accuracy, a scheme with a total mesh number of 674,905 is determined for the computational model. The overall mesh size is 1 mm, and the first grid length normal to the wall is 0.01 mm. The grid along the z-x plane is presented in Figure 7.

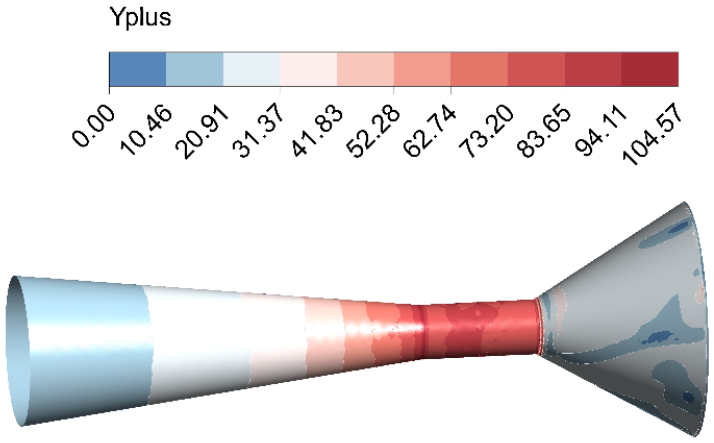


Figure 5. y^+ in CFD postprocessing.

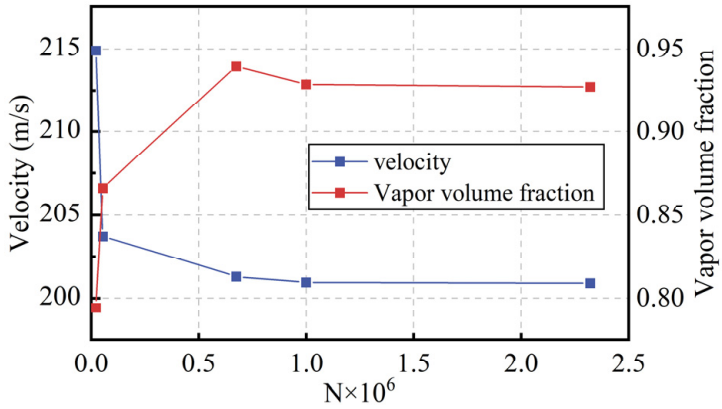


Figure 6. Mesh independence analysis.

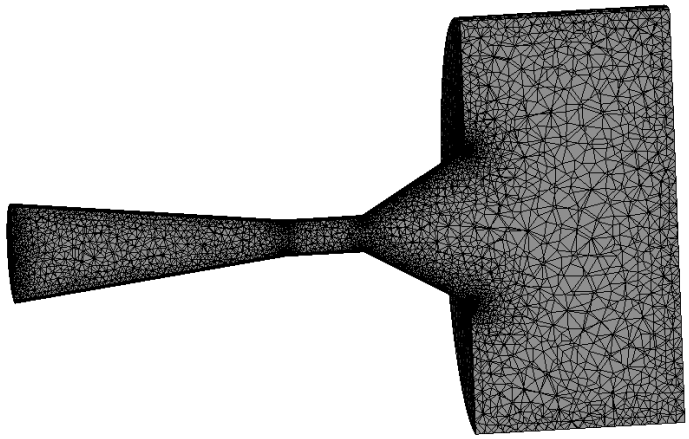


Figure 7. Grid along the z-x plane.

2.4. Boundary Condition

To simulate the internal and external flow fields of the submerged jet of the angular cavitation nozzle, incompressible liquid water is used as the first phase and gaseous water vapor as the second phase, and then the gas–liquid mass transfer is described by the cavitation model. The physical properties of the fluid are shown in Table 1. The user-defined density function (UDF) of water vapor is used to achieve mixture compressibility. The jet flow state is higher-Reynolds-number turbulence. According to the rated pressure and flow of the high-pressure pump, as well as the underwater submerged environment, the

boundary conditions are the pressure inlet and pressure outlet. Gravity is not considered. The parameters for boundary conditions are shown in Table 2.

Table 1. Physical properties of the fluid.

Physical Parameters	Value	Unit
Temperature	298.15	K
Water density	997.0	kg/m^3
Water kinematic viscosity	8.93×10^{-7}	m^2/s
Water dynamic viscosity	8.9×10^{-4}	Pa·s
Saturated vapor pressure	3169	Pa
Vapor density	UDF	kg/m^3

Table 2. Boundary condition setting.

Boundary Type	Location	Parameter	Value	Direction
Inlet	Nozzle inlet	Pressure	20 MPa	Normal
Opening	External flow field	Pressure (entrainment)	0.1 MPa	Zero gradient
Wall	Nozzle walls	Wall roughness	Smooth	No slip

2.5. Validation of the Simulation Method

Comparing the numerical model with experimental results of a similar nature, we have verified the correctness and feasibility of the model. Yang et al. [31] use high-speed photography experiments to capture the unsteady flow characteristics of a cavitation jet under three different expansion angles. Based on the structure parameter of the experiment, the model and method introduced above were used for simulation. The map of the jet axial velocity distribution and the axial vapor volume fraction distribution at $d/2$ with three expansion angles of the nozzle are shown in Figure 8. The results show that the nozzle with an expansion angle of 60° has the best cavitation effect, which is consistent with the experimental results.

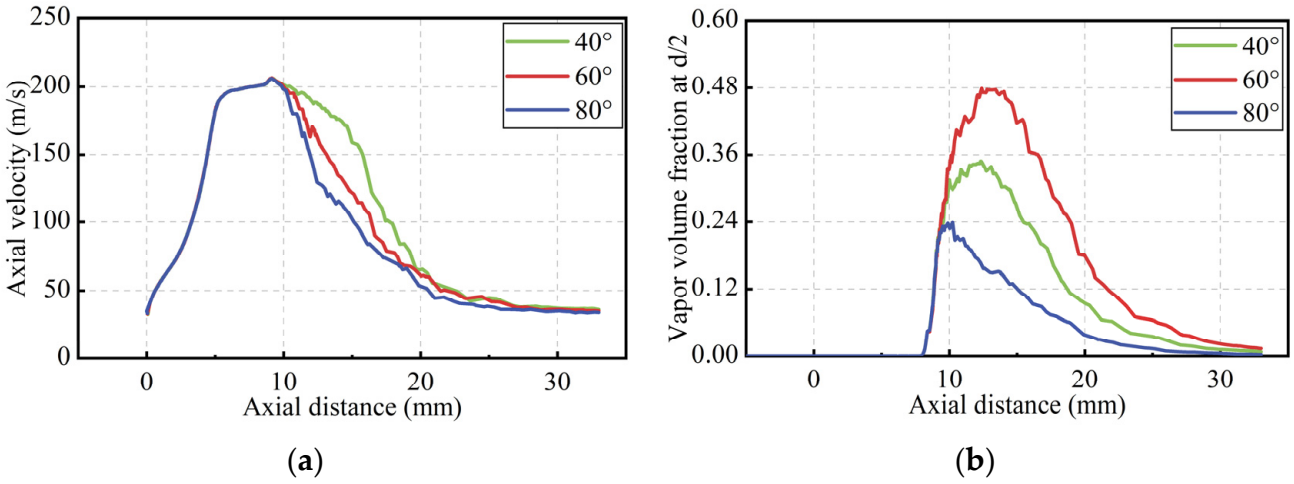


Figure 8. Effect of expansion angle on cavitation. (**a**) Axial velocity; (**b**) vapor volume fraction.

As shown in Figure 9, the development process corresponds to the first 350 µs period of cavitation. The blue area indicated by the dotted line in the figure indicates the main area of the bubble collapse [31]. Through the transient solution, the generation and shedding of the cavitation cloud are observed, as illustrated in Figure 10. Its development process is consistent with the experimental phenomenon. It has been established that cavitation vortex shedding was taking place in a periodical manner [13].

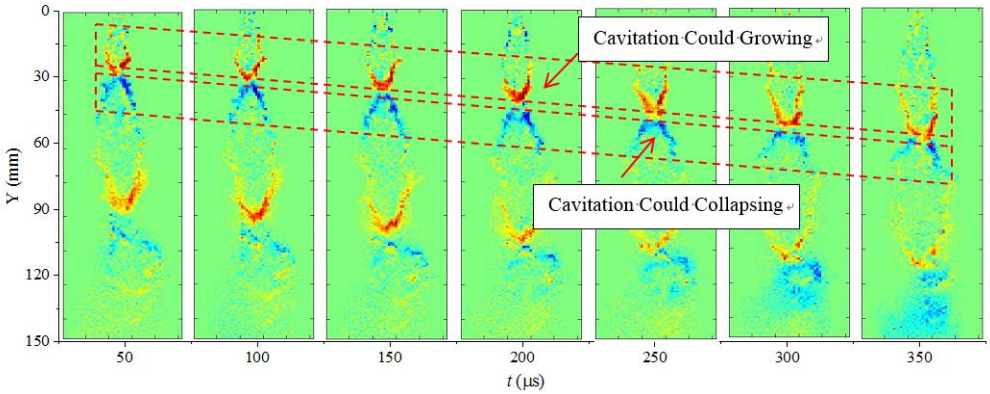


Figure 9. Cavitation process of experiment. Reprinted with permission from Ref. [31]. Copyright 2020, Mechanika.

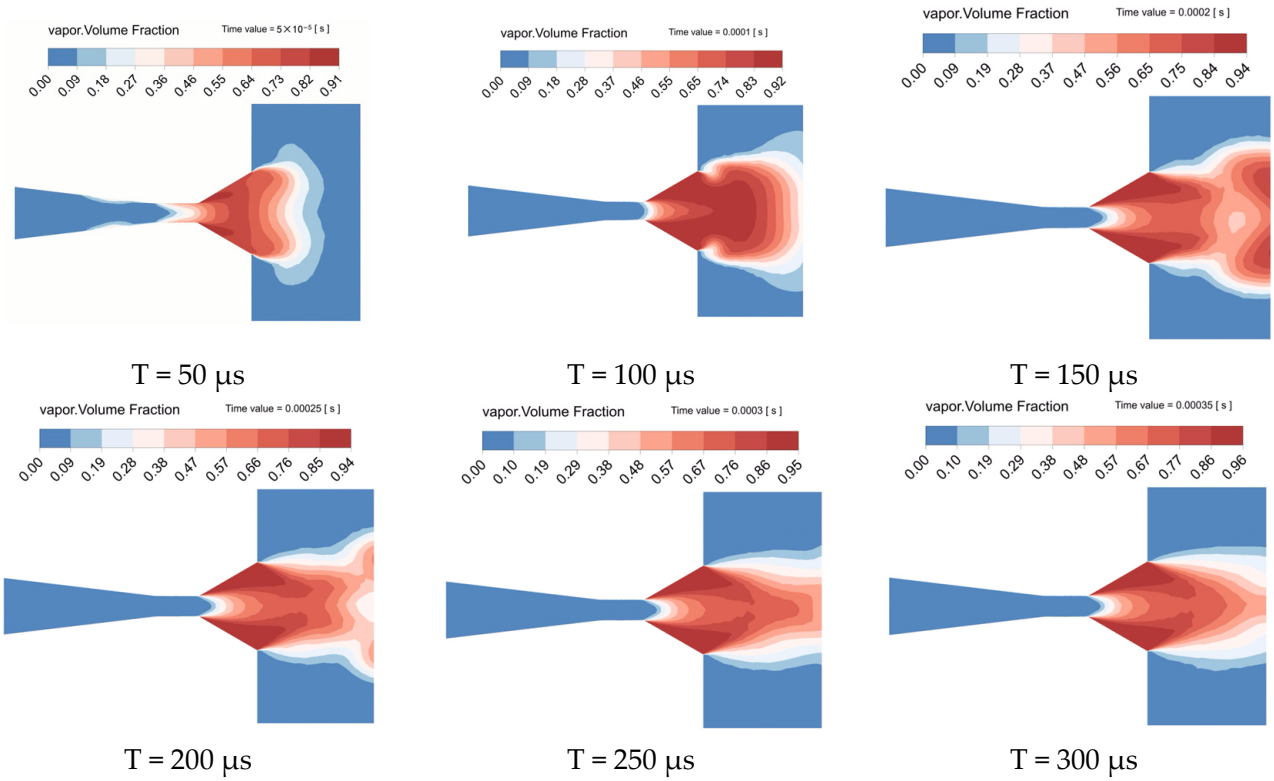


Figure 10. Cavitation process of transient simulation.

3. Results and Discussion

3.1. Preliminary Analysis of Nozzle Flow Field

In order to investigate the influence of nozzle structure on the cavitation effect of the angular cavitation nozzle, take the optimized nozzle structure parameters $\alpha = 13.5°$, $Ld = 3d$, $Le = 4d$, and $\beta = 60°$ for example to analyze the flow characteristics of the internal and external flow fields of the nozzle. In order to make a better presentation of the internal and external fields of the cavitation jet, the finally optimized structural parameters of the nozzle were selected as examples for analysis. The velocity cloud diagram, local velocity vector diagram, pressure cloud diagram, and vapor volume fraction cloud diagram of the angular cavitation nozzle on the z-x plane are shown in Figures 11–13. The axial velocity distribution and vapor volume fraction at $d/2$ of the angular cavitation nozzle are shown in Figures 14 and 15, respectively.

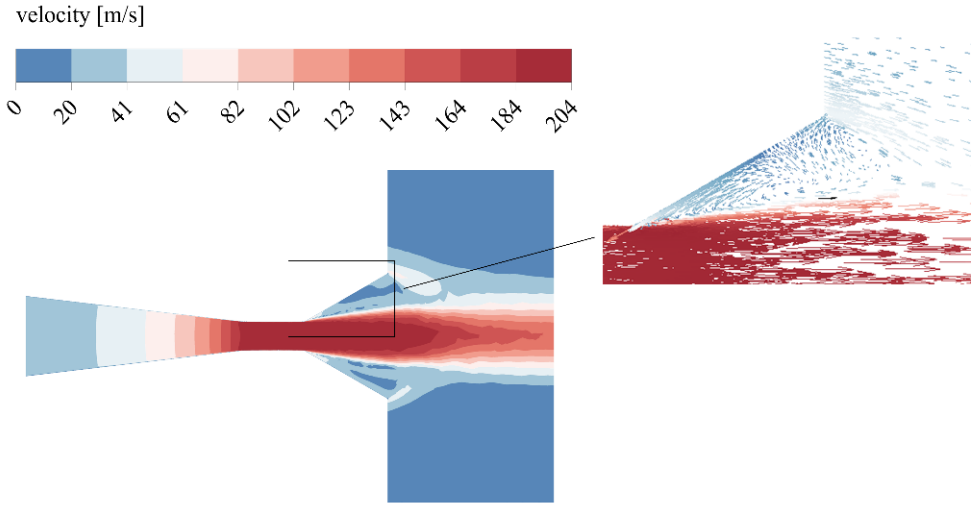


Figure 11. Velocity distribution of the angular cavitation nozzle.

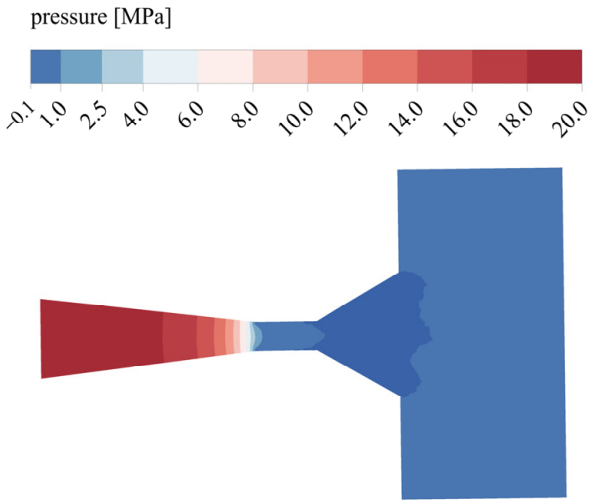


Figure 12. Pressure distribution of the angular cavitation nozzle.

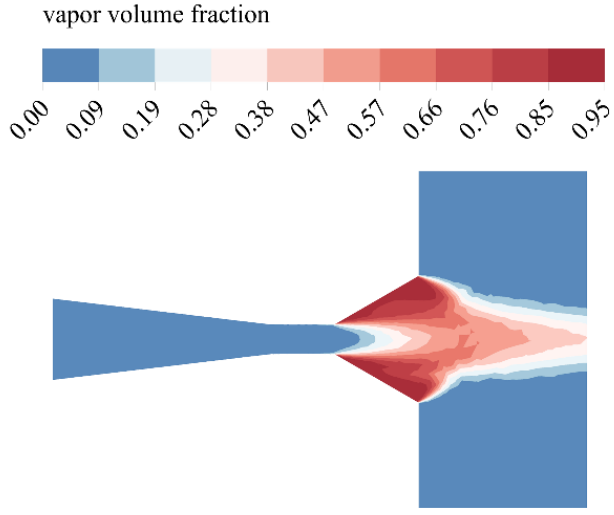


Figure 13. Vapor volume fraction variation of the angular cavitation nozzle.

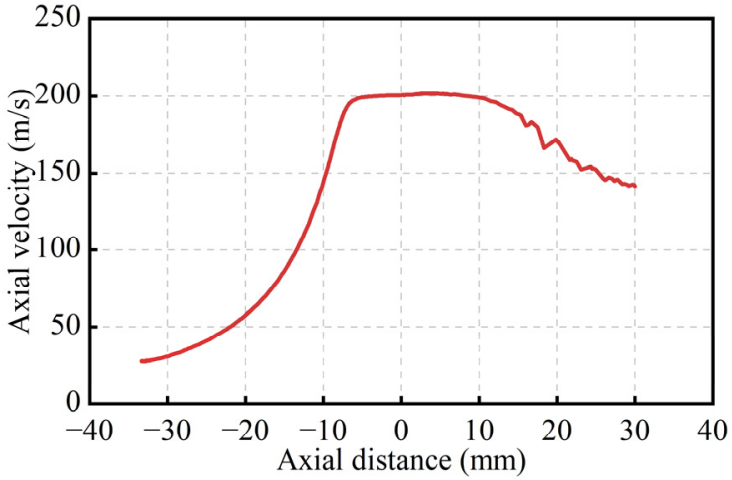


Figure 14. Axial velocity distribution.

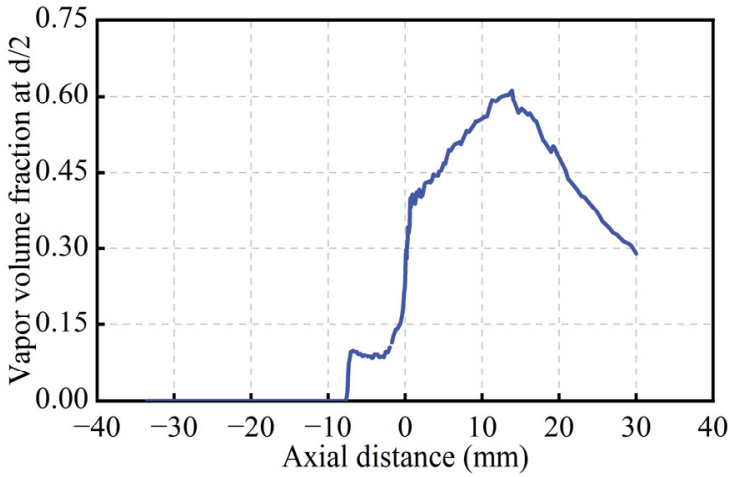


Figure 15. Axial vapor volume fraction distribution at $d/2$.

It can be seen from the velocity contour of the angular cavitation nozzle (see Figure 11) that the water flows from the nozzle inlet first and reaches the maximum velocity at the outlet of the cylindrical section through the continuous acceleration of the contraction section and the convergence of the cylindrical section. Then, the jet mixes vigorously with the liquid in the external flow field in the expansion section and develops into an isokinetic core section. The velocity is stable at 200 m/s. At the same time, the backflow phenomenon in the expansion section can also be observed (see the enlarged view of the local velocity vector in the black box in Figure 11). Finally, the jet velocity gradually decays to 0 m/s in the outer flow field with the extension of the jet distance.

According to the pressure contour of the angular cavitation nozzle (see Figure 12), the pressure decreases continuously from the nozzle inlet through the contraction section, the cylinder section, and the expansion section. In the expansion section of the nozzle, there is obviously a low-pressure area, which is lower than the atmosphere in the external flow field. With atmosphere as the reference pressure, the nozzle pressure is reduced from 20 MPa to 0 MPa and reaches −0.1 MPa in the expansion section. Referring to the angular cavitation nozzle velocity contour (see Figure 11), it can be seen that the pump pressure is converted into liquid kinetic energy, and a negative pressure zone is generated in the nozzle expansion section due to the strong shear action between the jet and the external flow field.

It can be seen from the vapor volume fraction contour in the angular cavitation nozzle (as shown in Figure 13) that there is no obvious generation of a cavitation cloud in the

nozzle contraction section and the cylinder section. The cavitation cloud is generated and developed in the expansion section and then enters the outflow field with the jet until it disappears. The formation and collapse of cavitation clouds are closely related to the pressure. Since the noncondensable gas that generates cavitation bubbles mainly exists in the liquid or on the liquid–solid interface, the cavitation clouds are generated and fall off from the near wall surface of the expansion section. Based on the 3D structure of the nozzle, the distribution of cavitation clouds generally presents a vortex ring shape, with a small vapor volume fraction in the central part and a large vapor volume fraction around it. This can be seen in some research [6,25]. Therefore, the axial vapor volume fraction distribution at $d/2$ can be used as the basis for judging the cavitation effect.

In order to easily distinguish the internal and external flow fields to explore the cavitation effect of the angular cavitation nozzle, set the outlet position of the cylindrical section at 0 mm on the axial distance of the velocity distribution and the vapor volume fraction distribution. Then, the contraction section is between −33.5 mm and −7.5 mm, the cylindrical section is between −7.5 mm and 0 mm, the expansion section is between 0 mm and 10 mm, and 10 mm to 30 mm is the area of the external flow field.

It can be seen from the axial velocity distribution of the angular cavitation nozzle (see Figure 14) that when the axial distance is less than −7.5 mm, the axial velocity of the jet increases with the extension of the axial distance. This is due to the convergence effect of the contraction section, which can enhance the flow velocity. When the axial distance is between −7.5 mm and 10 mm, the jet axial velocity is kept at about 200 m/s due to the constraint of the nozzle cylinder section. The length of the constant velocity core extends to the expansion section. When the axial distance is greater than 10 mm, the axial velocity of the jet decreases with the extension of the axial distance. At this time, the jet is in the outflow field, and the jet velocity is constantly attenuated due to doping with the surrounding liquid.

It can be seen from Figure 15 that when the axial distance is less than −7.5 mm, the steam volume fraction at $d/2$ is 0, indicating that there is no cavitation in the contraction section. When the axial distance is between −7.5 mm and 0 mm, the steam volume fraction at $d/2$ rises suddenly and decreases slowly with the increase in the axial distance. It indicates that the nozzle has cavitation in the cylindrical section, but the cavitation degree is too low, and the steam volume fraction is only about 0.1. Kumar et al. [17] compared the experimental and CFD-predicted results, thinking vapor is generated at the sharp entrance of the nozzle orifice, as expected. With the extension of the cylindrical section, the cavitation clouds decrease due to the weakening of the boundary layer. When the axial distance is within the range of 0 mm to 12 mm, the steam volume fraction at $d/2$ rises suddenly again and rises with the increase in the axial distance. As shown in Figure 12, the expansion section is conducive to the generation of cavitation clouds [11]. When the axial distance is more than 12 mm, the vapor volume fraction at $d/2$ decreases in the external flow field with the increase in the axial distance.

3.2. Influence of Contraction Section on Cavitation

To investigate the influence of the contraction section on the cavitation effect of the angular cavitation nozzle, keeping the remaining structural parameters constant and setting different contraction angles α (8°, 10°, 13.5°, 16°, and 20°), the axial velocity distribution of the jet inside the nozzle and the axial vapor volume fraction distribution at $d/2$ obtained from numerical simulations are shown in Figures 16 and 17, respectively. It is noted that the vapor fraction corresponding to different α shows roughly the same trend. It is because the angle of the contraction section (α) has less effect on the cavitation [25]. The change in α affects the bunching of the jet. On one hand, it causes energy loss and thus affects the jet velocity. On the other hand, it affects the flow state of the jet and hence affects the cavitation. However, the main cavitation region of the angular cavitation nozzle is located in the expansion section.

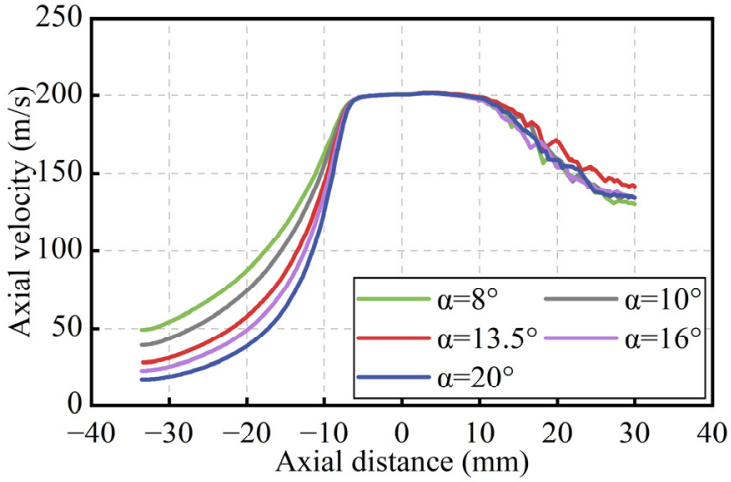


Figure 16. Effect of α on the fluid velocity.

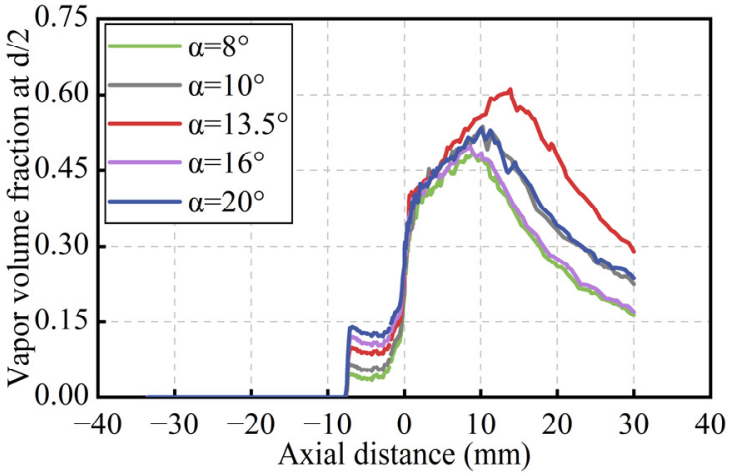


Figure 17. Effect of α on the cavitation.

According to the distribution of axial velocity at different α (see Figure 16), when the axial distance is less than -7.5 mm, the axial velocity of the jet decreases with the increase in α. This is because the larger the α, the greater the energy loss inside the contraction section and the smaller the jet velocity; in the range of axial distance between -7.5 mm and 10 mm, the axial velocity of the jet corresponding to different α is approximately the same, indicating that different α does not affect the maximum velocity of the jet. For an axial distance greater than 10 mm, the axial velocity of the nozzle jet with α of 13.5° is about 140 m/s at the edge of the external flow field (i.e., the value of the axial distance is 30 mm), which is the largest compared to the axial velocity of other α (about 130 m/s), but the overall difference is not significant.

From Figure 17, can be seen that when the axial distance is less than -7.5 mm, the steam volume fraction at $d/2$ corresponding to different α is 0, indicating that no cavitation occurs at this time. While the axial distance is in the range of -7.5 mm to 0 mm, the steam volume fraction at $d/2$ decreases with the reduction in α. The transition of the cylindrical section causes a sudden change in pressure, and the smaller α makes the first cavitation of the nozzle smaller. When the axial distance is greater than 0 mm, the steam volume fraction at $d/2$ of the nozzle with a value of 13.5° for α exceeds the volume fraction corresponding to the remaining α by a large margin. It indicates that the nozzle cavitation effect is best when α is 13.5°.

3.3. Influence of Cylinder Section on Cavitation

There is an optimal ratio between the length and the diameter of the nozzle cylindrical section [31,32]. Therefore, different dimensionless lengths of the cylindrical segment (Ld/d = 2, 2.5, 3, 3.5, 4) are set for numerical simulation, while other structural parameters are kept unchanged to explore the influence of the length of the cylinder section on the cavitation effect. In order to facilitate comparison, the nozzle inlet is set as 0 mm for drawing. The axial velocity distribution of the nozzle jet and the axial steam volume fraction distribution at $d/2$ are shown in Figures 18 and 19.

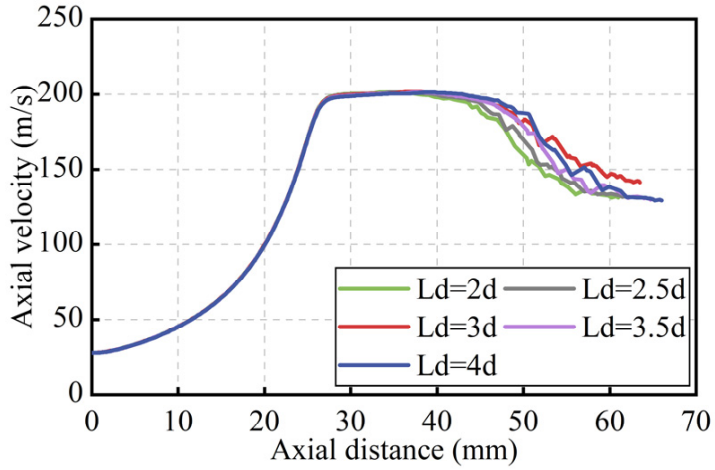


Figure 18. Effect of *Ld* on the fluid velocity.

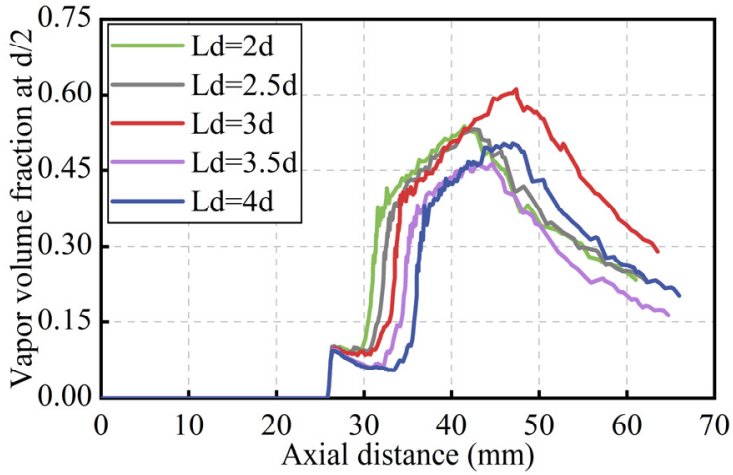


Figure 19. Effect of *Ld* on the cavitation.

As can be seen from Figure 18, when the axial distance is less than 40 mm (inside the nozzle), the axial velocity of the jet corresponding to different *Ld* is essentially the same, indicating that the change in *Ld* has little effect on the interior of the nozzle jet. But the longer the *Ld*, the longer the isokinetic nucleus. While the axial distance is greater than 40 mm (external flow field), the axial velocity of the jet corresponding to different *Ld* fluctuates up and down. The length of the dimensionless cylindrical section with a value of 3 has the largest axial velocity of the jet.

From Figure 19, it can be seen that when the axial distance is located in the contracted section (0 mm–26 mm), the steam volume fraction at $d/2$ for different *Ld* is 0. While the axial distance is within the cylindrical section (31 mm, 32.25 mm, 33.5 mm, 34.75 mm, and 36 mm at the end of the cylindrical section for different *Ld*), the steam volume fraction at $d/2$ decreases with the extension of *Ld*. As *Ld* increases, the fluid boundary layer gradually becomes thicker, making the cavitation in the cylindrical section smaller. When the axial

distance is located in the external flow field (41 mm, 42.25 mm, 43.5 mm, 44.75 mm, and 46 mm at the end of the nozzle for different *Ld*), the vapor volume fraction at the length of the dimensionless cylindrical section with a value of 3 is substantially higher than the one corresponding to the rest of parameters. It also has the best cavitation effect. This is different from the findings of SU et al. [32], who argue that when the length to diameter ratio is 2, the vapor fraction distribution region reaches the maximum. This shows that with the change in nozzle diameter, the length to diameter ratio corresponding to the best cavitation effect also changes, and the nozzle diameter should be confirmed first.

3.4. Influence of Expansion Section on Cavitation

3.4.1. Influence of Expansion Angle on Cavitation

To investigate the influence of the expansion angle on the cavitation effect of the angular cavitation nozzle, the rest of the structural parameters were kept constant, and different expansion angles β (30°, 40°, 60°, 80°, and 90°) were set for numerical simulation analysis. The map of the axial velocity distribution of the nozzle jet and the axial vapor volume fraction distribution at $d/2$ are shown in Figures 20 and 21, respectively.

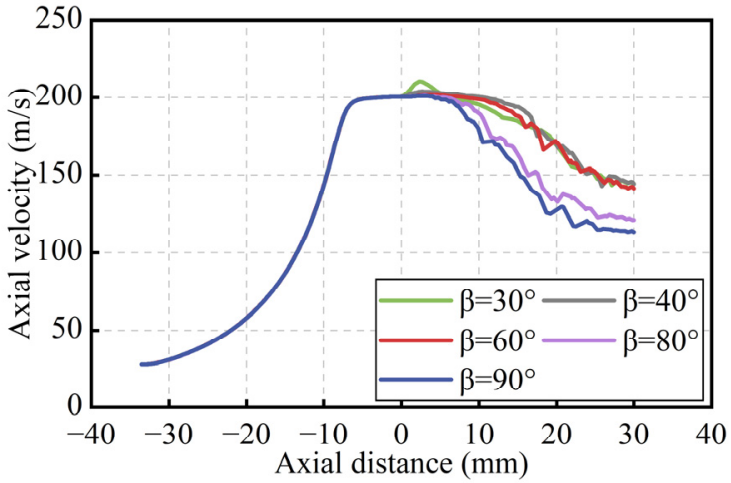


Figure 20. Effect of β on the fluid velocity.

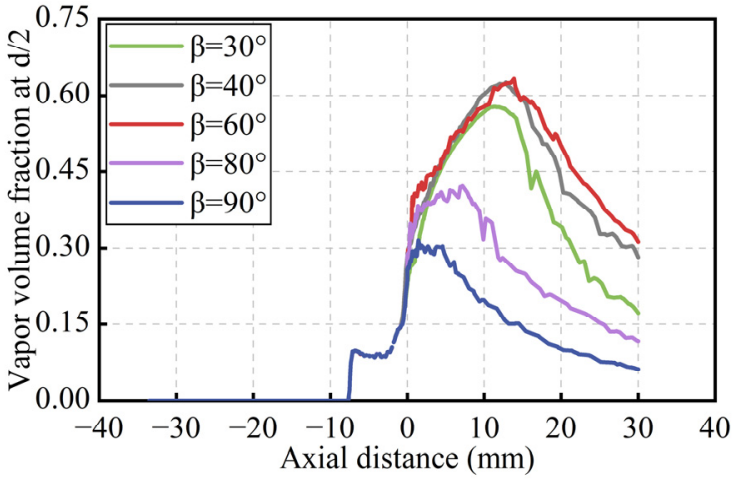


Figure 21. Effect of β on the cavitation.

According to the distribution of axial velocity at different β (Figure 20), it can be seen that when the axial distance is less than 0 mm, the axial velocity of the jet is approximately the same for different β. This is also in line with common sense that the change in the expansion section does not cause the axial velocity of the jet in the contraction section and

the cylindrical section. While the axial distance is greater than 0 mm, the maximum axial velocity of the jet decreases with the increase in β. It is due to the fact that the smaller the β, the more concentrated the jet energy, the smaller the energy loss, and the higher the jet velocity.

The distribution of the axial steam volume fraction at $d/2$ (Figure 21) shows that when the axial distance is less than 0 mm, the steam volume fraction at $d/2$ is basically the same for different β. While the axial distance is greater than 0 mm, the steam volume fraction at $d/2$ shows an ascending and then descending trend with the increase in β and reaches the maximum steam volume fraction when β is 60°. Therefore, a too-large or too-small β is not conducive to the generation of cavitation bubbles, and the nozzle with β = 60° has a better cavitation effect [33].

3.4.2. Influence of Expansion Section Length on Cavitation

To investigate the influence of the length of the expansion section on the cavitation effect of the angular cavitation nozzle, keeping the remaining structural parameters unchanged, numerical simulations were conducted by setting different dimensionless expansion section lengths [34] (Le/d = 3, 3.5, 4, 4.5, 5), and the results of the axial velocity distribution of the nozzle jet and the axial vapor volume fraction distribution at $d/2$ are shown in Figures 22 and 23, respectively.

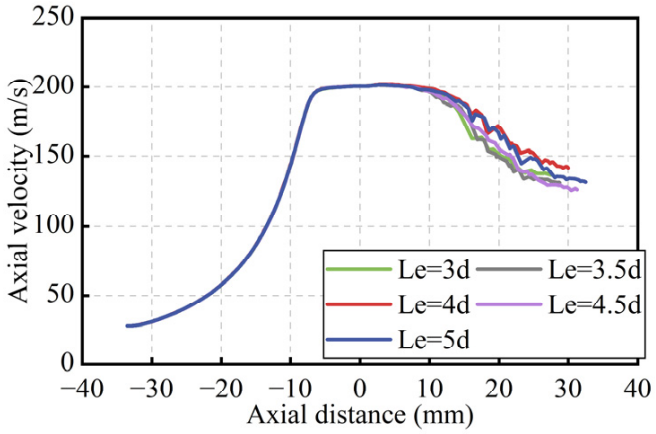


Figure 22. Effect of *Le* on the fluid velocity.

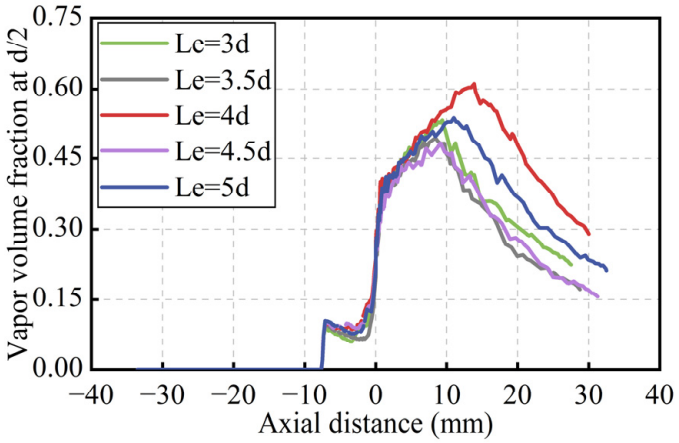


Figure 23. Effect of *Le* on the cavitation.

As can be seen from Figure 22, when the axial distance is less than 0 mm, the jet axial velocity corresponding to different Le is approximately the same, and there is essentially no effect on the jet velocity of the nozzle contraction section and the cylindrical section. While the axial distance is greater than 0 mm, the jet axial velocity corresponding to different

Le fluctuates within a certain range, in which the jet axial velocity of the length of the dimensionless expansion section with a value of 4 is the largest.

It can be seen from Figure 23 that when the axial distance is less than 0 mm, the steam volume fraction at $d/2$ corresponding to different Le is basically the same. When the axial distance is greater than 0 mm, the steam volume fraction at $d/2$ corresponding to different Le changes dramatically. If Le is too small, it is not conducive to the generation of cavitation bubbles, and the steam volume fraction is also small. Le should not be too large; otherwise, the growth of cavitation clouds is affected due to the fluid resistance. Therefore, the steam volume fraction is the largest and the cavitation effect is the best when $Le = 4d$.

4. Conclusions

Numerical simulation is a significant instrument to observe the flow features of the internal and external flow fields of angular cavitation nozzles, which can more effectively obtain the cavitation law of the jet. In this paper, combined with the influence of mixture density on cavitation, the structure of the cavitation nozzle has been optimized based on CFD technology, and a simulation model has been verified by relevant experiments. By considering the effect of angular cavitation nozzle structure on jet cavitation, it can be concluded that with a 20 MPa incident pressure and d = 2.5 mm, the maximum steam volume fraction of the angular cavitation nozzle can reach 0.95 when the nozzle structure parameters are $\alpha = 13.5°$, $Ld = 3d$, $Le = 4d$, and $\beta = 60°$. At this point, the nozzle has the best cavitation effect.

The cavitation jet of the angular cavitation nozzle presents a vortex ring shape. Cavitation bubbles are generated from the near wall surface of the expansion section where the maximum steam volume fraction appears. The steam volume fraction is small on the axis and gradually increases along the radial direction. It is more accurate and reliable to judge the cavitation effect by the axial steam volume fraction distribution at $d/2$.

The expansion section of the angular cavitation nozzle is the low-pressure area of the fluid and also the place where cavitation bubbles are generated and developed. Optimizing the structure of the expansion section can lead to a better cavitation effect.

Next, we will build an experimental platform guided by numerical simulation. On the one hand, we can further verify the feasibility of numerical simulation; on the other hand, we can obtain the best target distance of the nozzle through experiments to prepare for the application of the nozzle. The grid adaptation based on the gradient of the volume fraction indeed is a great meshing method. However, it is difficult to implement this grid adaptive technology in CFX software. This technology will be studied in our future work.

Author Contributions: Conceptualization, W.D. and W.L.; methodology, W.D.; software, W.D.; validation, W.D., L.Y. and W.L.; formal analysis, W.D.; investigation, W.D.; resources, W.D., L.Y. and W.L.; data curation, W.L.; writing—original draft preparation, W.D.; writing—review and editing, L.Y. and W.L.; visualization, W.D.; supervision, L.Y. and W.L.; project administration, L.Y.; funding acquisition, L.Y. All authors have read and agreed to the published version of the manuscript.

Funding: This research was funded by the National Key R&D Program of China, grant no. 2022YFB4702401 and Fuzhou Institute of Oceanography, grant no. 2021F11.

Institutional Review Board Statement: Not applicable.

Informed Consent Statement: Not applicable.

Data Availability Statement: The data presented in this study are available on request from the corresponding author.

Acknowledgments: The authors would like to thank the anonymous reviewers for their constructive suggestions, which comprehensively improved the quality of the paper. The authors also would like to thank the support from Fuzhou Ocean Research Institute and the support from the Fujian Provincial College Marine Engineering Equipment Design and Manufacturing Engineering Research Center.

Conflicts of Interest: The authors declare no conflict of interest.

References

1. Yang, Y.F.; Shi, W.D.; Li, W.; Chen, S.P.; Zhang, W.Q.; Pan, B. Experimental study on the surface property changes of aluminum alloy and stainless steel after impingement with submerged cavitation jet. *Strength Mater.* **2021**, *53*, 353–363. [CrossRef]
2. Bukharin, N.; El Hassan, M.; Omelyanyuk, M.; Nobes, D. Applications of cavitating jets to radioactive scale cleaning in pipes. *Energy Rep.* **2020**, *6*, 1237–1243. [CrossRef]
3. Ralys, A.; Moksin, V. Numerical simulation of a cavitating pulsating water jet used for removing contaminants from metal surfaces. *Trans. Famena* **2019**, *43*, 69–80. [CrossRef]
4. Soyama, H. Cavitating jet: A review. *Appl. Sci.* **2020**, *10*, 7280. [CrossRef]
5. Hu, J.K.; Tong, Z.M.; Xin, J.G.; Yang, C.J. Simulation and experiment of underwater robot jet cleaning based on cavitation jet technology. *J. Zhejiang Univ.—Sci. A (Appl. Phys. Eng.)* **2019**, *20*, 804–812. [CrossRef]
6. Tsutsumi, K.; Watanabe, S.; Tsuda, S.-I.; Yamaguchi, T. Cavitation simulation of automotive torque converter using a homogeneous cavitation model. *Eur. J. Mech. B-Fluids* **2016**, *61*, 263–270. [CrossRef]
7. Peng, C.; Tian, S.C.; Li, G.S. Joint experiments of cavitation jet: High-speed visualization and erosion test. *Ocean Eng.* **2018**, *149*, 1–13. [CrossRef]
8. Ylönen, M.; Franc, J.-P.; Miettinen, J.; Saarenrinne, P.; Fivel, M. Shedding frequency in cavitation erosion evolution tracking. *Int. J. Multiph. Flow* **2019**, *118*, 141–149. [CrossRef]
9. Hutli, E.; Nedeljkovic, M.; Bonyár, A. Cavitating flow characteristics, cavity potential and kinetic energy, void fraction and geometrical parameters-analytical and theoretical study validated by experimental investigations. *Int. J. Heat Mass Transf.* **2018**, *117*, 873–886. [CrossRef]
10. Li, F.Z.; Tan, Z.R.; Chen, L.T. Study on dynamic evolution of cavitation clouds and optimization of standoff distance in water cavitation peening. *J. Mech. Eng.* **2019**, *55*, 120–126. [CrossRef]
11. Wang, G.; Yang, Y.; Wang, C.; Shi, W.; Li, W.; Pan, B. Effect of nozzle outlet shape on cavitation behavior of submerged high-pressure jet. *Machines* **2022**, *10*, 4. [CrossRef]
12. Jablonská, J.; Kozubková, M.; Himr, D.; Weisz, M. Methods of experimental investigation of cavitation in a convergent-divergent nozzle of rectangular cross section. *Meas. Sci. Rev.* **2016**, *16*, 197–204. [CrossRef]
13. Mitroglou, N.; Stamboliyski, V.; Karathanassis, I.; Nikas, K.; Gavaises, M. Cloud cavitation vortex shedding inside an injector nozzle. *Exp. Therm. Fluid Sci.* **2017**, *84*, 179–189. [CrossRef]
14. Ibanez, I.; Zeqiri, B.; Hodnett, M.; Frota, M. Cavitation-erosion measurements on engineering materials. *Eng. Sci. Technol.* **2020**, *23*, 1486–1498. [CrossRef]
15. Yang, Y.; Shi, W.; Tan, L.; Li, W.; Chen, S.; Pan, B. Numerical research of the submerged high-pressure cavitation water jet based on the RANS-LES hybrid model. *Shock Vib.* **2021**, *2021*, 6616718. [CrossRef]
16. Ran, Z.L.; Ma, W.X.; Liu, C.B. 3D cavitation shedding dynamics: Cavitation flow-fluid vortex formation interaction in a hydrodynamic torque converter. *Appl. Sci.* **2021**, *11*, 2798. [CrossRef]
17. Kumar, A.; Ghobadian, A.; Nouri, J.M. Assessment of cavitation models for compressible flows inside a nozzle. *Fluids* **2020**, *5*, 134. [CrossRef]
18. Chen, Y.Z.; Hu, Y.H.; Zhang, S.L. Structure optimization of submerged water jet cavitating nozzle with a hybrid algorithm. *Eng. Appl. Comput. Fluid Mech.* **2019**, *13*, 591–608. [CrossRef]
19. Wu, Z.B.; Wang, Y.Y.; Zhang, S.; Lantao, L.; Wenjuan, W. Numerical simulation of cavitation performance of nozzles of different shapes. *Fluid Mach.* **2020**, *48*, 36–41.
20. Wang, L.; Shi, D.; Yang, Z.; Li, G.; Ma, C.; He, D.; Yan, L. Numerical simulation and experimental research of cavitation nozzle based on equation curve. *Water Supply* **2021**, *21*, 2261–2272. [CrossRef]
21. Zhang, Y.; Wu, X.; Li, G.; Hu, X.; Hui, C.; Tan, Y.; Huang, H. Study on erosion performance of swirling cavitating jet for natural gas hydrate. *J. Cent. South Univ. (Sci. Technol.)* **2022**, *53*, 909–923.
22. Omelyanyuk, M.; Ukolov, A.; Pakhlyan, I.; Bukharin, N.; El Hassan, M. Experimental and numerical study of cavitation number limitations for hydrodynamic cavitation inception prediction. *Fluids* **2022**, *7*, 198. [CrossRef]
23. Hu, B.; Wang, H.; Liu, J.; Zhu, Y.; Wang, C.; Ge, J.; Zhang, Y. A numerical study of a submerged water jet impinging on a stationary wall. *J. Mar. Sci. Eng.* **2022**, *10*, 228. [CrossRef]
24. Kamisaka, H.; Soyama, H. Enhancing the aggressive intensity of a cavitating jet by introducing water flow holes and a long guide pipe. *J. Fluids Eng.* **2021**, *143*, 031201. [CrossRef]
25. Yang, Y.; Li, W.; Shi, W.; Zhang, W.; AEl-Emam, M. Numerical investigation of a high-pressure submerged jet using a cavitation model considering effects of shear stress. *Processes* **2019**, *7*, 541. [CrossRef]
26. Brennen, C.E. *Cavitation and Bubble Dynamics*; Cambridge University Press: Cambridge, UK, 1995.
27. Peng, G.; Mori, M.; Tazaki, T.; Oguma, Y. Numerical simulation of unsteady cloud cavitation: A comparative study of compressible mixture models. *IOP Conf. Ser. Earth Environ. Sci.* **2019**, *240*, 062043. [CrossRef]
28. Erdem, K.; Bilal, C. Evaluating the influence of turbulence models used in computational fluid dynamics for the prediction of airflows inside poultry houses. *Biosyst. Eng.* **2019**, *183*, 1–12.
29. Dai, Y.; Zhang, X.; Zhang, G.; Cai, M.; Zhou, C.; Ni, Z. Numerical analysis of influence of cavitation characteristics in nozzle. *Flow Meas. Instrum.* **2022**, *85*, 102172. [CrossRef]

30. Gao, Z.X.; Jiang, C.W.; Lee, C.H. Improvement and application of wall function boundary condition for high-speed compressible flows. *Sci. China-Technol. Sci.* **2013**, *56*, 2501–2515. [CrossRef]
31. Yongfei, Y.A.N.G.; Wei, L.I.; Weidong, S.H.I.; Chuan, W.A.N.G.; Zhang, W. Experimental study on submerged high-pressure jet and parameter optimization for cavitation peening. *Mechanika* **2020**, *26*, 346–353.
32. Yuan, M.; Li, D.; Kang, Y.; Shi, H.; Pan, H. Characteristics of oscillation in cavity of helmholtz nozzle generating self-excited pulsed waterjet. *Chin. J. Mech. Eng.* **2022**, *35*, 73. [CrossRef]
33. Su, Y.Q.; Shi, J.F.; Wang, Y.H. Numerical simulation of cavitation of water jet nozzle based on realizable k-ε model. *Mechanika* **2022**, *28*, 12–18. [CrossRef]
34. Soyama, H. Enhancing the aggressive intensity of a cavitating jet by means of the nozzle outlet geometry. *J. Fluids Eng.* **2011**, *133*, 101301. [CrossRef]

Disclaimer/Publisher's Note: The statements, opinions and data contained in all publications are solely those of the individual author(s) and contributor(s) and not of MDPI and/or the editor(s). MDPI and/or the editor(s) disclaim responsibility for any injury to people or property resulting from any ideas, methods, instructions or products referred to in the content.